JOURNAL OF PROPULSION AND POWER
Vol. 10, No. 4, July–Aug. 1994

Experimental and Computational Results for the External Flowfield of a Scramjet Inlet

D. A. Ault* and D. M. Van Wie†
The Johns Hopkins University Applied Physics Laboratory, Laurel, Maryland 20723

A two-dimensional hypersonic scramjet inlet has been investigated in a combined experimental and analytical program aimed at addressing the fundamental issues related to the design of scramjet inlets. The experimental portion of the program was conducted in the Calspan 48-in. shock tunnel at Mach 10 and 13. The computational analysis was conducted using a two-dimensional parabolized Navier-Stokes computational fluid dynamics (CFD) code. This article addresses the issues concerned with the flow over the external forebody of the inlet which consists of a blunted wedge followed by an isentropic compression. The pressure and heat transfer distributions over the forebody are investigated for ranges of Reynolds number, Mach number, wall-to-freestream temperature ratio, and nose bluntness. Comparison of the test results and CFD predictions show that good agreement for the heat transfer distributions is achieved. However, the predicted pressure distribution on the forward blunted wedge was consistently underpredicted by 18–33% relative to the experimental measurements. Several phenomena were investigated in an attempt to explain the discrepancy between predicted and measured pressure distributions, including classical viscous leading-edge interactions, blunt leading-edge interactions, slip flow effects, flow condensation, flow angularity, and facility Mach number uncertainty. Although the discrepancy in the forebody pressure ratios could be caused by a combination of the factors listed above, a deficiency in the modeling of the viscous interaction region by the CFD codes and facility flow angularity are shown to be the strongest contributors.

Nomenclature

C = $(\rho\mu)_w/(\rho\mu)_e$
C_h = Stanton number
h_t = total enthalpy
Kn = Knudsen number
L = characteristic length
M = Mach number
P = pressure
R_n = model nose radius
Re = Reynolds number
T = temperature
X = model axial station
Y = model elevation
Z = model lateral station
λ = nitrogen molecular mean free path
$\bar{\chi}$ = viscous interaction correlation parameter

Subscripts
b = body
e = boundary-layer edge condition
t = stagnation value
tr = transition
w = wall condition
θ = momentum thickness
$0, \infty$ = freestream condition

Introduction

A COMBINED experimental and analytical program has been completed to address the fundamental issues regarding the design and analysis of two-dimensional hypersonic inlets. The issues investigated include the effects of Reynolds number, Mach number, wall-to-freestream temperature ratio, and nose bluntness. The goal of the program was to increase confidence in the design and analysis of these inlets. This increased knowledge is required for the development of high-speed, air-breathing engines for future aircraft and missile systems.

The experimental portion of the program was conducted in the 48-in. shock tunnel at the Arvin/Calspan Advanced Research Center in Buffalo, New York. This shock tunnel uses a contoured nozzle with replaceable nozzle throat blocks to provide a range of freestream Mach numbers. Mach numbers between 9.9–13.1 were tested under this program. The shock tunnel was operated such that freestream total pressures up to 4600 psia and total temperatures up to 3300°R were achieved. The facility run times for all tests were in the range of 6–9 ms. For this experimental program, all runs were conducted using nitrogen as the test medium.

The experimental program consisted of 19 runs conducted at the four sets of freestream conditions shown in Table 1. These test conditions were used to assess the effects of Reynolds number, Mach number, and wall-to-freestream temperature ratio on the inlet operation. Thirteen of the nineteen runs were completed for condition A which corresponds to the maximum Reynolds number which could be obtained at Mach 10.4 in the shock tunnel. Two runs were conducted at each of the other three test conditions. The effect of Reynolds number on the inlet operation was investigated using condition B which corresponded to a lower Reynolds number compared to condition A. Note the freestream Mach number and wall-to-freestream temperature ratio were approximately the same between conditions A and B. The effect of the model wall-to-freestream temperature ratio was investigated using condition C compared to condition B. Because the model wall temperature does not change appreciably during the few milliseconds of a test, the freestream temperature for condition C was raised to create a factor of 2 change in the temperature ratio. Note that the Mach and Reynolds numbers are approximately the same for conditions B and C. The inlet performance was investigated at a higher Mach number using

Presented as Paper 92-5100 at the AIAA 4th International Aerospace Planes Conference, Orlando, FL, Dec. 1–4, 1992; received Feb. 13, 1993; revision received Nov. 10, 1993; accepted for publication Nov. 19, 1993.

*Associate Staff Engineer. Member AIAA.
†Principal Staff Engineer. Member AIAA.

Table 1 Test conditions

Condition	M_0	Re/ft	P_{t_0}, psia	T_{t_0}, °R	P_0, psia	T_0, °R	Runtime, ms
A	10.39	5.7×10^6	4585	1894	0.088	87.7	6
B	10.22	2.2×10^6	1686	1835	0.034	87.6	9
C	9.89	1.9×10^6	4140	3311	0.092	177.4	6
D	13.14	1.3×10^6	4560	2849	0.016	86.6	6

Table 2 Aerodynamic contour

X, in.	Y, in.
$0 < X < 8.3566$	$Y = (\tan 5°)X$
$8.3566 < X < 23.3561$	$Y = 9.8870 \times 10^{-5}(X - 8.3566)^3 + 7.3687 \times 10^{-4}(X - 8.3566)^2 + 0.08749(X - 8.3566) + 0.7311$
$23.3561 < X < 35.0$	$Y = (\tan 10°)(X - 23.3561) + 2.54284$

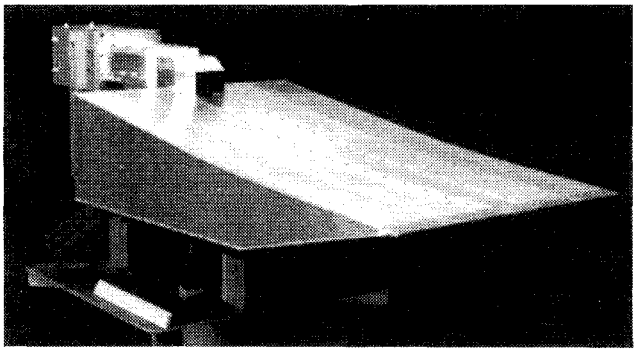

Fig. 1 Photograph of inlet model.

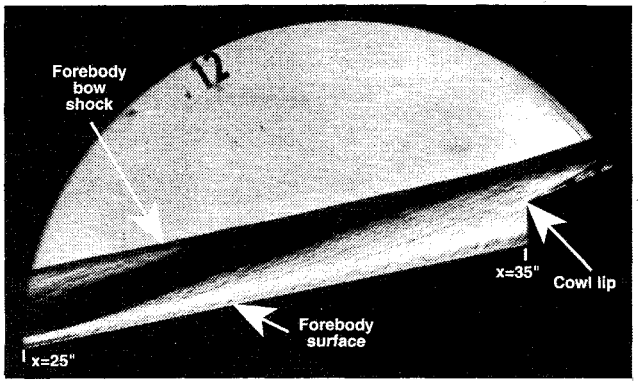

Fig. 2 Schlieren photograph of the forebody flowfield near the cowl lip. $M_0 = 10.4$, Re/ft $= 5.7 \times 10^6$, $T_w/T_0 = 6.1$, and $R_n = 0.005$ in.

condition D. Effects of nose bluntness were investigated at conditions A and D. All tests were conducted with the model at zero angle of attack.

The analytical portion of this program was completed using a series of computational fluid dynamics (CFD) codes that include a viscous shock layer (VSL) code which solves the blunt nose region, and an upwind-differencing parabolized Navier-Stokes (PNS) code which solves the flowfield over the external forebody.[1] All codes used in this investigation assume two-dimensional flow of a perfect gas. The boundary layers can be either laminar, transitional, or fully turbulent. For the calculations presented herein, the starting point of transition and the length of the transition zone input to the CFD codes were selected to best match the experimental data. Turbulent flows were modeled with a two-equation K-ε model. The wall temperature was held constant at 530°R.

The computational grid contained 150 points in the vertical direction, with between 20–32 points maintained in the subsonic region of the wall boundary layer, and approximately 1600 points axially. Axial grid spacing is bounded by the laminar sublayer thickness for a minimum step size and the Courant-Friedrichs-Lewy (CFL) criterion for a maximum. For the results shown, the maximum step size was also limited to five nose radii. Peak y^+ values for the first grid point off the wall were between 1.4–1.8 for all solutions, with values of y^+ generally maintained between 0.5–0.8. Default damping levels built into the codes were utilized.

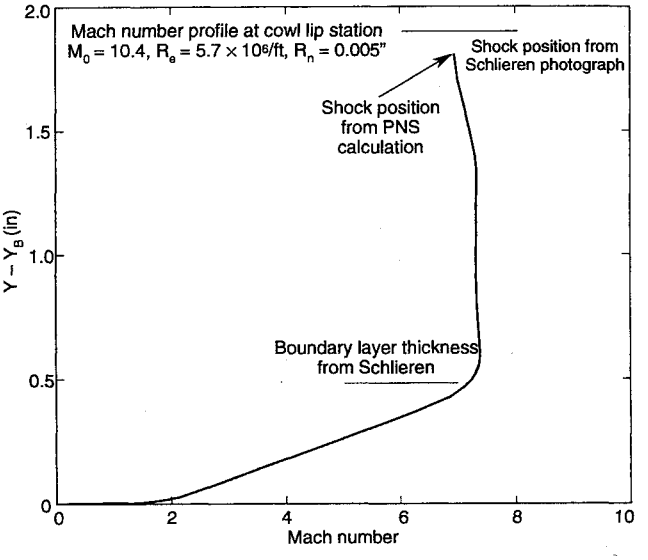

Fig. 3 Comparison of test results with PNS predictions for the flowfield at the cowl lip plane.

Model Description

A photograph of the model is shown in Fig. 1. The aerodynamic contour consists of a blunted 5-deg wedge followed by an isentropic compression region which turns the flow an additional 5 deg. Table 2 gives the (X, Y) coordinates of the model aerodynamic surface in inches measured from an origin located at the theoretical sharp tip of the forebody.

The effect of forebody nose radius was investigated using a replaceable nose section. Forebody nose radii R_n of 0.005 and 0.100 in. were tested. Two rows of instrumentation were located at ±2.5 in. off of the model centerline, $Z = \pm 2.5$ in., with alternating pressure and heat transfer gauges. The forebody pressure and heat transfer distributions were used to verify the two-dimensionality of the flowfield.

Comparison of Experimental Results and CFD Predictions

A typical schlieren photograph of the forebody flowfield in the vicinity of the cowl lip is shown in Fig. 2. The test conditions corresponding to this photograph are $M_0 = 10.4$, $Re = 5.7 \times 10^6$/ft, $T_w/T_0 = 6.1$, and $R_n = 0.005$ in. The forebody bow shock, isentropic compression field, and forebody boundary layer can be seen in this photograph. Comparisons of the bow shock position and boundary-layer height between the PNS calculations and that measured from the schlieren photograph are shown in Fig. 3 on the Mach number profile obtained from the PNS calculation at the cowl lip

plane. Although measurement of boundary-layer thickness from a schlieren photograph is not usually very accurate, good qualitative agreement in boundary-layer thickness and bow shock location were achieved. The CFD code predicts the bow shock at 95% (−0.1-in. difference) of the distance from the body as observed in the schlieren photograph.

A comparison between PNS calculations and test results of the forebody pressure and heat transfer distributions is shown in Fig. 4 for condition A, with $M_0 = 10.4$, $Re = 5.7 \times 10^6$/ft, $T_w/T_0 = 6.1$, and $R_n = 0.005$ in. In this and subsequent figures, the test data are represented by discrete symbols, and the results obtained from the CFD analysis are shown as solid or dashed lines. The error bars on the test data represent the standard deviation in the measurements which were obtained over the 10 runs that were conducted at this test condition. Note that the standard deviation of the measurements varies considerably at different axial stations. This variation is caused by either a difference in the quality of the individual measurement gauge, or by local variations in the flowfield. For example, the large standard deviation in heat transfer in the transition region is probably caused by slight movement of the transition location from run to run. In general, many factors other than repeatability affect the overall accuracy of a measurement. Typically, the accuracy of pressure measurements made in shock tunnels is approximately 5%, whereas the accuracy of the heat transfer measurements is approximately 10%.

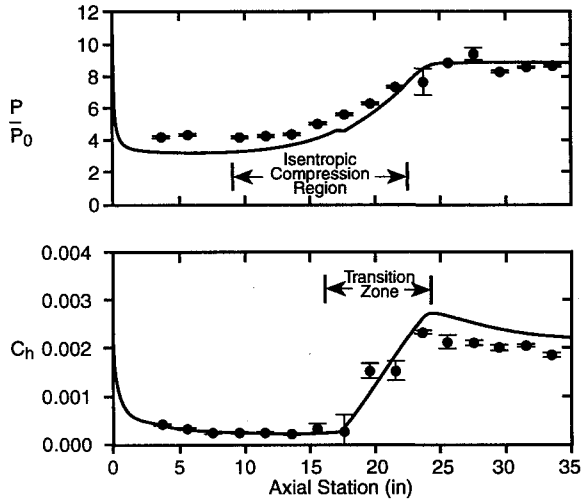

Fig. 4 Comparison of test results with PNS predictions for the forebody pressure and heat transfer distributions. $M_0 = 10.4$, Re/ft $= 5.7 \times 10^6$, $T_w/T_0 = 6.1$, and $R_n = 0.005$ in.

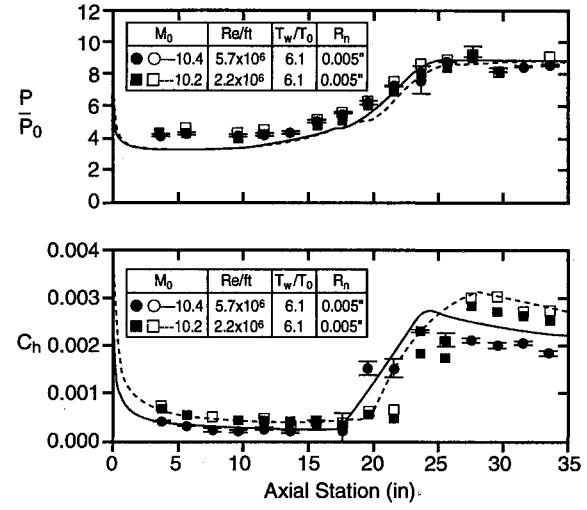

Fig. 5 Effect of Reynolds number on the forebody pressure and heat transfer distributions.

As seen in the PNS calculations shown in Fig. 4, the pressure distribution over the forebody consists of a nose region characterized by a rapidly decreasing pressure from the stagnation region, a pressure plateau corresponding to the flow over the first ramp, an isentropic compression region, and a final pressure plateau corresponding to the region downstream of the isentropic compression section. The results indicate that the pressure on the first ramp was underpredicted by approximately 30%, while the pressure obtained after the isentropic compression shows good agreement between theory and test. This underprediction of the pressure on the first ramp was a phenomenon seen in all of the tests and is discussed later in this article.

The heat transfer distributions over the forebody shown in Fig. 4 consist of a laminar flow region followed by a section where the isentropic compression and boundary-layer transition are both present. Downstream of the isentropic compression region, the boundary layer appears to be fully turbulent. The results show excellent agreement between the calculations and test data for the heat transfer in the laminar region. Transition began at an axial location 17 in. downstream of the leading edge. The PNS analysis indicated that $Re_\theta/M_e = 139$ at this location. The length of the transition zone was approximately 7 in. The results also show that the PNS code overpredicts the heat transfer in the turbulent region by approximately 20%. This difference between PNS calculations and test results could possibly be decreased with further refinement in the position and length of transition or improvements in the PNS grid.

The effects of Reynolds number on the forebody pressure and heat transfer distributions are shown in Fig. 5. Because only two runs were conducted at condition B, error bars based on the standard deviation are not presented. The test results from the two condition B cases at $M_0 = 10.2$, $Re = 2.2 \times 10^6$/ft, $T_w/T_0 = 6.1$, and $R_n = 0.005$ in. are both plotted as the open and filled square symbols and compared to the results obtained at condition A. The test results and computational analysis both show a general insensitivity of the nondimensional pressure distribution to Reynolds number, whereas the Stanton number distribution is 40–50% higher for the lower Reynolds number condition. The test results for the lower Reynolds number condition again show the underprediction of pressure on the first ramp and the overprediction of the heat transfer in the turbulent region on the final ramp. The experimental location of the beginning of transition moved 4–5 in. downstream for the lower Reynolds number condition. The value of Re_θ/M_e at this location is 96. This small movement in the transition location for a factor of 2.6 change in freestream Reynolds number suggests that the adverse pres-

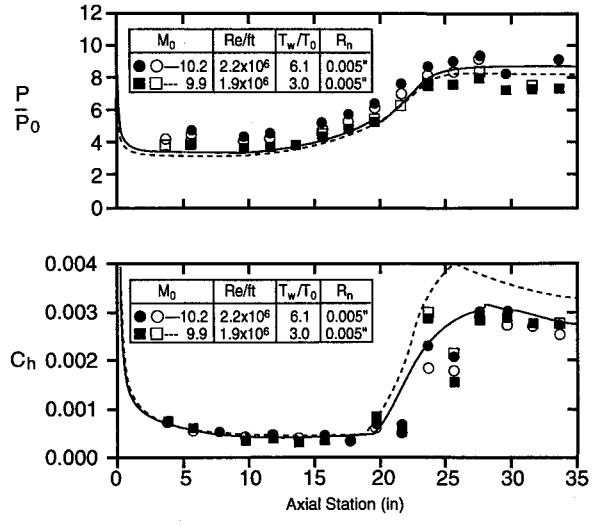

Fig. 6 Effect of wall-to-freestream temperature ratio on the forebody pressure and heat transfer distributions.

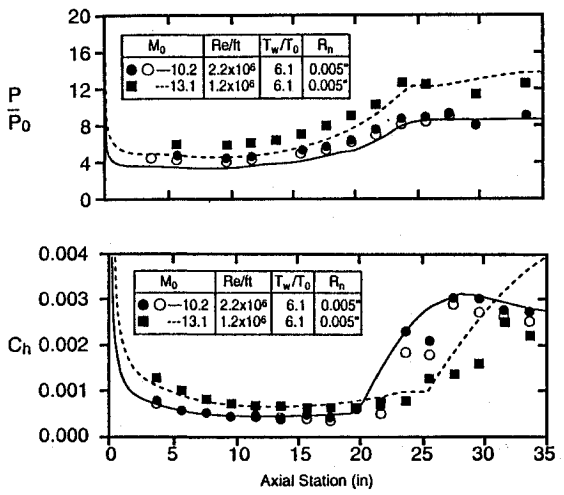

Fig. 7 Effect of freestream Mach number on the forebody pressure and heat transfer distributions.

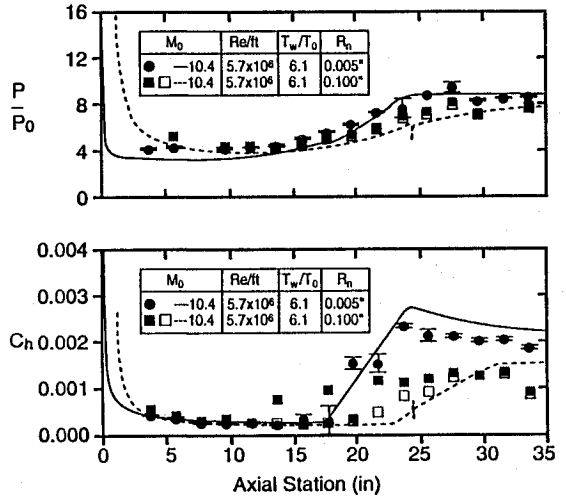

Fig. 8 Effect of nose radius on forebody pressure and heat transfer distributions.

sure gradient in the isentropic compression field has a destabilizing effect on the boundary layer. Note that for condition B, the onset of transition for the PNS solution was moved upstream relative to the experimental results to better match the heat transfer in the fully turbulent region.

The effects of the wall-to-freestream temperature ratio on the forebody pressure and heat transfer distributions are shown in Fig. 6. The test results for the two condition C cases at $M_0 = 9.9$, $Re = 1.9 \times 10^6$/ft, $T_w/T_0 = 3.0$, and $R_n = 0.005$ in. are compared with the results obtained at condition B. The results show that a change in the wall-to-freestream temperature ratio from 6.1 to 3.0 has a small effect on the pressure distribution and practically no effect on the Stanton number distribution or the location and length of transition. The results do show that, for the lower wall-to-freestream temperature ratio, condition C, the pressure measured on the forward ramp was much closer to that predicted. In addition, the test data does not show much sensitivity of the Stanton number distribution to the wall-to-freestream temperature ratio in the turbulent flow region over the final ramp while the PNS code predicted a measurable difference.

The effects of the freestream Mach number on the forebody pressure and heat transfer distributions are shown in Fig. 7 by comparing tests conducted at conditions B and D for test cases where $R_n = 0.005$ in. Note that $M_0 = 10.2$ and $Re = 2.2 \times 10^6$/ft for condition B, while $M_0 = 13.1$ and $Re = 1.2 \times 10^6$/ft for condition D, so that these results are caused by a combination of changes in Mach and Reynolds numbers.

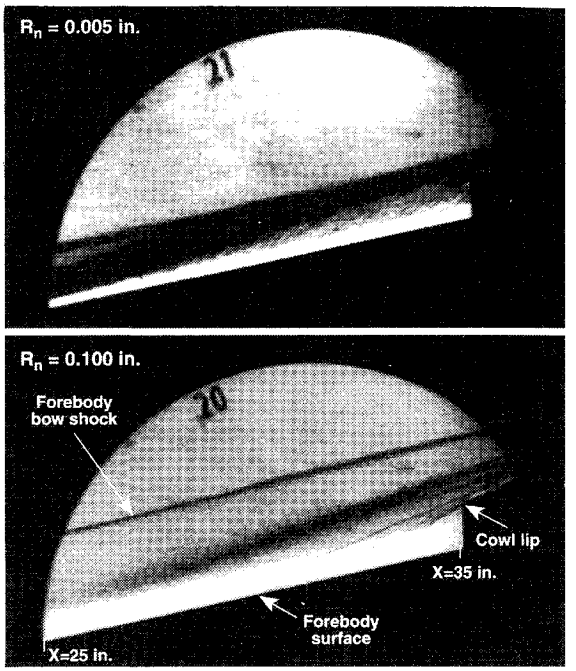

Fig. 9 Schlieren photographs showing the effect of nose radius on the inlet flowfield. $M_0 = 13.1$, Re/ft $= 1.3 \times 10^6$, and $T_w/T_0 = 6.1$.

However, as shown in Fig. 5, a change in Reynolds number from 2.2 to 5.7 $\times$ 10^6/ft has little effect on the experimental or computational pressure ratios. Assuming this is also true for the range of Reynolds number given in Fig. 7, nearly all of the change in the pressure ratio shown in Fig. 7 is due to the change in Mach number. As expected, the pressure ratio for the forebody flowfield is higher at the Mach 13.1 condition compared to the Mach 10.2 condition. The pressure ratio on the first ramp obtained in the test program is again higher than would be expected based on the CFD calculations, although the overall compression ratio for the Mach 13.1 condition compares favorably with the PNS calculations. The test data shows that the experimental transition location for the Mach 13.1 condition moved aft approximately 2 in. relative to the Mach 10.2 condition. The heat transfer distribution indicates that the transition length has increased significantly for the Mach 13.1 condition, and the value of Re_θ/M_e is 71 at the beginning of transition. Based on a review of the external and internal heat transfer measurements, the boundary layer for the Mach 13.1 condition appears to be transitional (not fully turbulent) at the cowl lip station.

The effect of nose bluntness on the forebody pressure and heat transfer distributions is shown in Fig. 8 for tests at condition A. In the PNS calculations of the flowfield, the increase in nose bluntness from 0.005 to 0.100 in. created a larger region of overpressurization on the first forebody ramp, and modified the isentropic compression field such that the overall forebody compression ratio was reduced. Qualitatively, these features of the flowfield are evident in the measured pressure distributions. The increased nose bluntness caused the transition to move aft approximately 5 in. to a point where the value of Re_θ/M_e was 168, but the transition length is approximately the same as for the sharper nose case. The heat transfer levels in the turbulent region on the final ramp were approximately 30% lower with the blunt nose. The blunt nose case does show some asymmetrical flow characteristics with the experimental transition approximately 7 in. farther forward on one side of the model centerline.

The effect of nose bluntness on the inlet operation at Mach 13.1 is shown dramatically in the schlieren photographs presented in Fig. 9. These photographs correspond to identical test conditions, $M_0 = 13.1$ and $Re = 1.2 \times 10^6$/ft, with $R_n = 0.005$ in. in the upper photograph and $R_n = 0.100$ in. in

Table 3 Summary of boundary-layer transition results

M_0	Re/ft	T_w/T_0	R_n, in.	X_{tr}, in.	L_{tr}, in.	$(Re_\theta/M_e)_{tr}$
10.39	5.7×10^6	6.1	0.005	17.0	7.0	139
10.39	5.7×10^6	6.1	0.100	22.5	8.5	168
10.22	2.2×10^6	6.1	0.005	19.0	9.0	96
9.89	1.9×10^6	3.0	0.005	18.5	7.0	100
13.14	1.3×10^6	6.1	0.005	25.0	>10.0	71
13.14	1.3×10^6	6.1	0.100	35.0	——	91

the lower photograph. The inlet operation for the test with $R_n = 0.005$ in. was as expected, with the forebody bow shock, isentropic compression, and boundary layer clearly evident. For the test with $R_n = 0.100$ in., the external flowfield, including the bow shock and isentropic compression field, was displaced outward by a much thicker boundary/entropy layer. In addition, the existence of several oblique shock waves located immediately upstream of the cowl lip indicates that the inlet was unstarted for the test with $R_n = 0.100$ in. It is believed that this unstart was caused when the forebody boundary layer did not transition prior to reaching the adverse pressure gradient associated with the internal inlet compression field. When the laminar boundary layer separated, an inlet unstart resulted. For this particular Mach 13.1 test condition, changing from $R_n = 0.005$ in. to $R_n = 0.100$ in. caused a dramatic change in the inlet operation, with the larger nose radius resulting in an inlet unstart.

A summary of parameters relating to the forebody transition data is provided in Table 3. For the calculation of Re_θ, the edge condition was taken at a location where $h_t/(h_t)_0 = 0.99$. For all test conditions, transition began at a location where the value of Re_θ/M_e was between 71–168.

Investigation of Forward Ramp Pressure Ratio Discrepancy

One phenomenon which was consistently present throughout the test program was the underprediction of the pressure on the forward ramp of the inlet forebody. The overpressurization of the forebody ramp relative to the PNS and inviscid calculations is summarized in Table 4 where it is seen that the difference between PNS calculations and experimental results is as much as 33%. This discrepancy was especially puzzling in that the measured overall forebody compression ratios were in general agreement with calculations, as were the heat transfer levels in the laminar region of the forward forebody ramp. Because the calculation of the pressure distribution on a blunted wedge in hypersonic flow should be relatively straightforward, this trend was very troubling and provoked additional investigation.

Using results from tests at condition A with $R_n = 0.005$ in. as the baseline, several issues were investigated in an attempt to explain the pressure ratio discrepancy on the forebody. The initial considerations focused on the quality of the flowfield within the Calspan 48-in. shock tunnel. The PNS codes were utilized to determine that an increase in Mach number from 10.387 to 13.387, or a flow angle such that the model is at 1.5-deg angle of attack, is required to match the pressure ratio on the forward ramp measured in the test. Although an error of 3.0 in Mach number is unlikely, a small local flow angle in the test section is possible. Figure 10 shows the average condition A test data, the initial PNS prediction, and the effect of the changes in Mach number to 13.387 and angle of attack to 1.5 deg. As shown in the figure, an increase in the Mach number or angle of attack for the CFD solutions causes the test and predicted pressure ratios to be in good agreement on the blunted wedge and forward isentropic compression region. However, the overall compression ratio at the cowl lip is overpredicted by up to 60% relative to the test data. The change in Mach number or angle of attack has a negligible effect on the heat transfer distribution in the laminar region; however, the heat transfer is overpredicted

Table 4 Comparison of measured and predicted forebody pressures

Condition	$(P_w/P_0)_{meas}$	$(P_w/P_0)_{calc}$ PNS/inviscid	% Difference PNS/inviscid
A	4.26	3.30/3.14	29/36
B	4.27	3.30/3.09	28/38
C	3.77	3.20/2.99	18/26
D	6.00	4.5/4.06	33/48

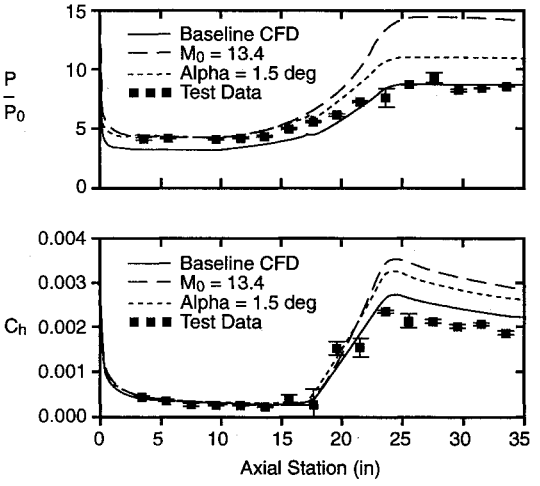

Fig. 10 Effect of changes in the freestream Mach number and flow angle on the forebody pressure and heat transfer distributions.

relative to the test data by up to 60% in the turbulent region. It is important to note that while the changes in Mach number and flow angularity imposed on the CFD solutions are uniform, any changes of these parameters in the wind tunnel could vary locally. A local variation in the freestream conditions could explain why the forebody forward ramp pressure is underpredicted, whereas the overall forebody compression ratio is accurately predicted.

A number of other phenomena were investigated in an attempt to explain the discrepancies between test measurements and CFD calculations. The first issue investigated was the possibility that slip flow effects could be contributing to the discrepancy. In regions of very low density, where the molecular mean free path λ is "large," gases do not behave as a continuum and the equations used by CFD codes are not valid. The parameter that governs this is the Knudsen number, $Kn = \lambda/L$, where L is a characteristic dimension of the body. For this problem, the characteristic length was taken as the length to the first pressure tap, 0.305 ft. The mean free path for nitrogen evaluated for condition A is 6.04×10^{-6} ft, so the Knudsen number is equal to 1.97×10^{-5}. If $Kn < 0.03$, slip effects usually can be ignored and the continuum Navier-Stokes equations are valid. Hence, condition A is well within the bounds of a continuum flow model, and slip flow should not be a source of the discrepancy in the measured and predicted pressure ratios on the forebody.

Flow condensation was also investigated as a possible source of the discrepancy between the measured and predicted pressure ratios. Because it was desired to obtain the maximum

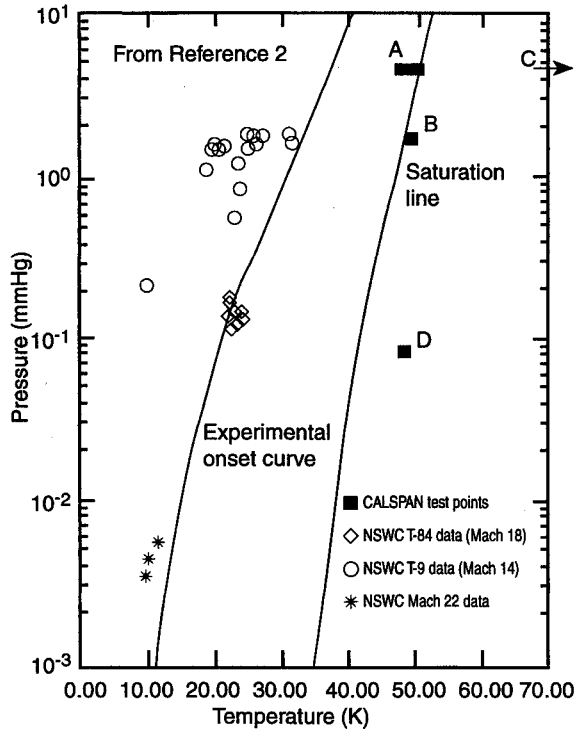

Fig. 11 Compilation of data for the onset of condensation.

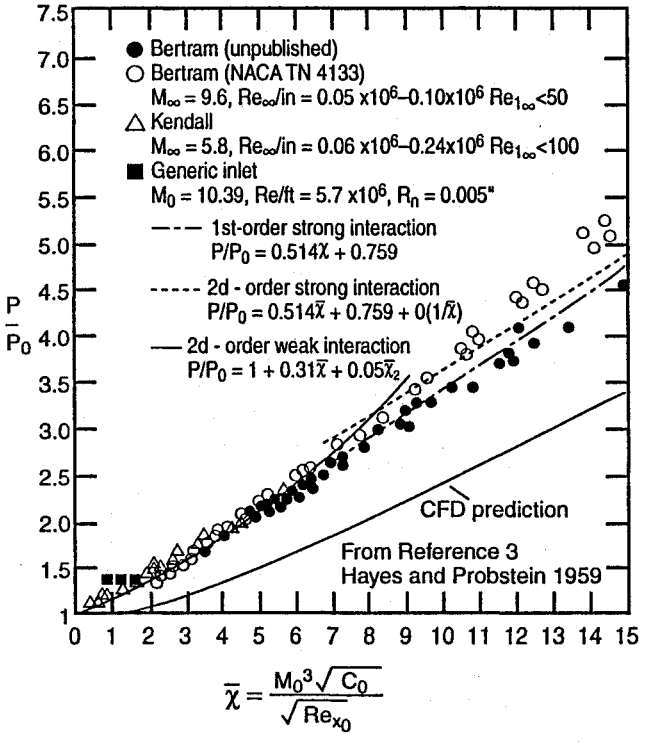

Fig. 12 Viscous interaction induced pressure rise.

possible Reynolds number, the facility was run at freestream temperatures very close to the saturation temperature for tests at conditions A, B, and D. Figure 11, from Ref. 2, shows test data for the onset of condensation in various hypersonic facilities. The results show that condensation usually does not occur until the freestream temperature is lowered approximately 20 K below the saturation temperature. The test conditions for this experimental program have been overlaid on Fig. 11. Although conditions A and B lie close to the theoretical saturation line, they are far from the onset of condensation as indicated from test data. Based on these considerations, the possibility that flow condensation affected the inlet flowfield was ruled out.

The fact that the calculated pressure distribution is closer to the measured value at condition C compared to the other conditions may provide some indication of the source of the pressure ratio discrepancy. Because the wall temperature is effectively colder for condition C ($T_w/T_0 = 3.0$ for condition C compared to $T_w/T_0 = 6.1$ for conditions A and B), the boundary layer is thinner on the forebody for this condition. Hence, the pressure induced on the forebody due to the growth of the forebody boundary layer would be smallest for this condition. One possible explanation for this discrepancy in forebody pressures is that the PNS codes are not correctly calculating the pressure increment induced by the boundary-layer displacement effect. By considering the PNS calculations relative to the inviscid calculations, it is seen that the viscous-induced pressure increment must be underpredicted by a factor of from 3 to 7 for this to be the explanation.

Figure 12, taken from Ref. 3, shows the correlation of induced pressure due to boundary-layer growth. Three condition A data points from the initial 5-deg wedge along with the induced pressure predicted by the PNS code have been overlaid on the figure. The induced pressure ratios were obtained by dividing the measured and CFD-predicted pressure ratios by the inviscid pressure rise for a 5-deg wedge. Note that all measured pressures are well within the weak interaction region, the region where the coupling between boundary-layer growth and the inviscid flowfield is weak and the induced pressure ratio is small. Although the test data does not exhibit the expected trend of increasing induced pressure ratio with decreasing length (increasing $\bar{\chi}$), the data points are within the scatter of other test data. Also of note is that the CFD-predicted induced pressure ratio is consistently lower than the correlation. This makes a strong argument that a large part of the discrepancy in the measured and predicted pressure ratios may be due to a problem with the CFD code underpredicting the induced pressure ratio due to viscous interactions. This problem could be due to either a deficiency of the VSL code used in the nose region or inadequate grid resolution.

Inaccuracies in the CFD modeling of the blunt leading-edge effects were also evaluated as a cause for the pressure ratio discrepancy. Although there is an effect on the first several pressure taps with the 0.1-in. nose, the first pressure tap ($X = 3.66$ in.) is 732 nose radii downstream of the leading edge for the 0.005-in. nose, which is well outside the region of blunt leading-edge effects. Therefore, the discrepancy in forebody pressure ratios is not caused by blunt leading-edge effects for the sharp nose ($R_n = 0.005$ in.) case under consideration.

Conclusions

Accurate prediction and verification of pressure and heat transfer distributions on wind-tunnel models is necessary to gain confidence in CFD prediction methods and the implementation of these tools to vehicle system design. A combined experimental and analytical hypersonic inlet test program has been completed to investigate the issues associated with hypersonic inlet design and verification. The effects of Reynolds number, Mach number, wall-to-freestream temperature ratio, and nose bluntness on the external flowfield of a two-dimensional hypersonic inlet have been investigated.

Several issues have been investigated to determine the cause of a discrepancy in measured and predicted forebody pressure ratios on the inlet external forebody. Issues dealing with facility flow quality, such as Mach number uncertainty, flow angularity, flow condensation, and slip flow effects were investigated. Issues dealing with the PNS prediction of the pressure ratio, such as viscous leading-edge interactions and blunt leading-edge interactions were also investigated. Although the pressure ratio discrepancy could be caused by a combi-

nation of several factors listed above, it is shown that this discrepancy is most likely caused by a local facility flow angularity and/or an underprediction of the viscous leading-edge interaction by the PNS CFD code.

Acknowledgments

This work was sponsored by the Aeropropulsion and Power Directorate at Wright Laboratory with Wade Smith and Dean Petters as project managers. The experimental work at the Calspan Corporation was conducted under the guidance of Michael Holden and Don Adams. The PNS codes utilized in the work were developed and distributed by the Science Applications International Corporation in Valley Forge, Pennsylvania.

References

[1]Krawczyk, W. J., and Harris, T. B., "Computational Models for the Analysis/Design of Hypersonic Scramjet Components," AIAA Paper 86-1596, June 1986.

[2]Lederer, M., Yanta, W., Ragsdale, W., Hudson, S., and Griffith, W., "Condensation in Hypersonic Nitrogen Wind Tunnels," AIAA Paper 90-1392, June 1990.

[3]Hayes, W. D., and Probstein, R. F., *Hypersonic Flow Theory*, Academic Press, New York, 1959.